# **Inorganic Chemistry**

pubs.acs.org/IC Article

# Evaluation of Ce-MOFs as Photoanode Materials for the Water Oxidation Reaction: The Effect of Doping with [Ru(bpy)(dcbpy)(H<sub>2</sub>O)<sub>2</sub>]<sup>2+</sup> Catalyst

Naduvile Purayil Dileep, Jully Patel, and Yulia Pushkar\*



Cite This: https://doi.org/10.1021/acs.inorgchem.3c04632



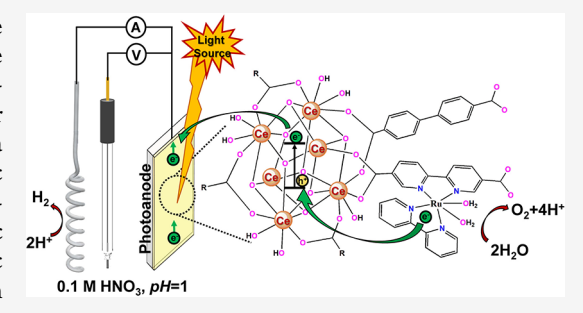
**ACCESS** I

Metrics & More

Article Recommendations

Supporting Information

**ABSTRACT:** Artificial photosynthesis stands out as a highly effective method for harnessing sunlight to produce clean and renewable energy. The light-absorbing properties, chemical stability, and high redox activity of Cebased metal—organic frameworks (MOFs) make them attractive materials for visible-light-driven water splitting. Currently, Ce-based MOFs remain a relatively underexplored system for photocatalytic water oxidation in acidic media. In this study, we synthesized a Ce-MOF with different linkers (1,4-benzenedicarboxylic acid, tetrafluoroterephthalic acid, 2-nitroterephthalic acid, 2,2'-bipyridine-5,5'-dicarboxylic acid, and 4,4'-biphenyldicarboxylic acid), which exhibit light-absorbing capability. Ce-based MOFs doped with  $[Ru(bpy)(dcbpy)(H_2O)_2]^{2+}$  (MOF-1 and MOF-2) water oxidation catalyst



showed an enhanced photoelectrocatalytic current of  $\sim 10^{-4}~{\rm A\cdot cm^{-2}}$  at pH = 1, which is comparable with the  $[{\rm Ru}({\rm bpy})({\rm dcbpy})({\rm H_2O})_2]^{2+}$ -doped MIL-126 Fe-based MOF. We also demonstrated the long-term durability of Ru-doped Ce-MOFs for photoelectrocatalytic water oxidation under acidic conditions. The as-synthesized MOFs were analyzed with powder X-ray diffraction (PXRD), Raman spectroscopy, Fourier transform infrared spectroscopy (FTIR), UV-visible diffuse reflectance spectroscopy, scanning electron microscopy (SEM), and electric conductivity measurements. This study contributes to the development of cost-effective materials for sustainable photocatalytic water splitting processes.

# INTRODUCTION

The increasing global population and growing economy have led to a significant increase in energy demand. To meet this demand, we have primarily relied on fossil fuels; however, the consumption of fossil fuels increases greenhouse gas emissions, notably carbon dioxide (CO<sub>2</sub>), introducing the foreboding presence of global warming and climate change. Therefore, there is an urgent need for green and clean energy sources as replacements for fossil fuels.<sup>1-5</sup> Harnessing sunlight through artificial photosynthesis has emerged as a highly effective approach for producing carbon-free and environmentally friendly fuel. Specifically, water splitting represents the most promising pathway for advancing the development of clean and renewable energy. 1,2 The main challenge in hydrogen production through water splitting is the complex multielectron water oxidation reaction (WOR). To efficiently convert sunlight into chemical energy, we need photocatalytic materials that can absorb visible light photons, generate charge-separated states with suitable redox potentials, have high activity for water splitting and are high durable in the harsh chemical conditions of WOR. Currently, iridium and ruthenium oxide-based water oxidation catalysts (WOCs) are among the most active and stable electrocatalysts for water oxidation at low pH, but their high cost motivates the pursuit of more cost-effective alternatives with fewer limitations.6Furthermore, the development of photoelectrocatalysts is challenging because it necessitates the dual performance of the material as a photoabsorber and as a catalyst. MOFs have emerged as a promising category of porous materials with tremendous potential for innovative applications in photocatalysis. Their unique crystalline structures, characterized by metal ions or clusters linked by organic ligands, provide remarkable surface area and tunable properties. <sup>11–13</sup>

In the past decade, Zr-based MOFs have been studied for their photocatalytic performance under UV-light.  $^{14,15}$  However, the wide band gap of Zr-based MOFs ( $\sim\!3.7$  eV) does not allow for photoactivity in the visible range.  $^{16,17}$  Fe-based MOFs (Fe-MIL-101, Fe-MIL-126, Fe-MIL-100, Fe-MIL-88, and Fe-MIL-53), all containing Fe $_3$ O units with carboxylate ligands, are capable of absorbing the visible light.  $^{18,19}$  Our group recently reported the incorporation of catalytically active  $\left[\text{Ru}(\text{bpy})(\text{dcbpy})(\text{H}_2\text{O})_2\right]^{2+}$  WOC into an Fe-based MIL-126, demonstrating the efficient photoelectrochemical water

Received: December 29, 2023 Revised: April 10, 2024 Accepted: April 11, 2024



oxidation at pH = 1.6 While being photoactive, Fe-based MOFs, such as Fe-MIL-101, Fe-MIL-126, Fe-MIL-100, Fe-MIL-88, and Fe-MIL-53, have low electrical conductivity, which possibly limits the overall performance of the photoanodes. Hence, this study analyzes the effect of the replacement of the Fe-based MOFs with Fe<sub>3</sub>O photoactive units with a variety of Ce-based MOFs with all  $Ce^{IV}$  Ce<sub>6</sub>-nodes while using the same  $[Ru(bpy)(dcbpy)(H_2O)_2]^{2+}$  WOC. The electrical conductivity of the Ce-MOFs was systematically assessed in the study but was also found to be low.

Motivation to evaluate Ce-based MOFs<sup>20</sup> is compelling, as interest in these materials has witnessed rapid growth in recent years due to their unique advantages, such as their relatively low cost, high redox activity, photoabsorbing properties, and environmentally friendly synthesis.<sup>21–29</sup> The appeal of Ce-MOFs lies in their combination of microporosity, the  $Ce^{III}/^{IV}$ redox properties, and the presence of low-energy 4f orbitals, granting them the capability to exhibit exceptional photo/electrocatalytic properties. <sup>29–31</sup> The ability to tailor Ce-MOFs with different functional groups, control their bandgap, and prevent the recombination of photogenerated electrons and holes makes them an interesting material for efficient visible light-responsive catalysts. <sup>22,23,31</sup> For instance, Meicheng Wen et al. found that cerium-ion-doped chromium-based aminefunctionalized MOF (CeMIL-101(Cr)) is suitable for H<sub>2</sub> production from ammonia borane under visible light irradiation.<sup>32</sup> Pd/CeMIL-101(Cr) exhibited improved catalytic activity compared to Pd/MIL-101(Cr) under visible light irradiation due to efficient light-induced charge separation and transfer of photogenerated electrons from MOF to Pd. 32 Recently, Shan Dai et al. reported different Ce-based MOFs (Ce-UiO-66-X (X = H, Br, NH<sub>2</sub>, NO<sub>2</sub>, COOH), Ce-DUT-67, and Ce-MOF-808) and investigated their photocatalytic activity for both hydrogen evolution reaction (HER) and oxygen evolution reaction (OER) under simulated sunlight irradiation.<sup>23</sup> Ce-UiO-66-NH<sub>2</sub> and Ce-UiO-66-NO<sub>2</sub> showed the best HER and OER activity, respectively, at  $pH \sim 7.23$ Interestingly, these Ce-UiO-66-based materials were found to be more active than their zirconium analogues, likely due to the low-lying 4f orbitals of Ce<sup>4+</sup> ions that favor the ligand-tometal charge transfer.<sup>23</sup> These studies show the light-absorbing properties, chemical stability, and high redox activity of Cebased MOFs. 23,32

Here, we explore Ce-based MOFs for photocatalytic water oxidation in acidic media. Ce-MOF (Ce-UiO-66 (Ce-BDC), Ce-UiO-66-F<sub>4</sub> (Ce-BDC-F<sub>4</sub>), Ce-UiO-66-NO<sub>2</sub> (Ce-BDC-NO<sub>2</sub>), Ce-UiO-66-dcbpy (Ce-dcbpy), and Ce-UiO-66-bpdc (Ce-bpdc), with different linkers (BDC = 1,4-benzenedicarboxylic acid, BDC-F<sub>4</sub> = tetrafluoroterephthalic acid, BDC-NO<sub>2</sub>=2-nitroterephthalic acid, dcbpy = 2,2'-bipyridine-5,5'dicarboxylic acid, and bpdc = 4,4'-biphenyldicarboxylic acid) were prepared (Figure 1). All materials exhibited lightabsorbing capability; Ce-bpdc and Ce-bpdc-dcbpy(1:1) materials allowed the incorporation of [Ru(bpy)(dcbpy)-(H<sub>2</sub>O)<sub>2</sub>]<sup>2+</sup> using various synthetic routes (Figure 2). Ru-WOC enhanced prolonged photoelectrocatalytic activity toward water oxidation in acidic media (pH = 1). We have achieved the long-term stabilization of Ce-MOF materials on fluorine-doped tin oxide (FTO) glass electrodes for sustained photoelectrocatalytic water oxidation in acidic conditions with the use of a proton-conductive Nafion membrane. The assynthesized Ce-MOFs were analyzed with powder X-ray diffraction (PXRD), Raman spectroscopy, Fourier transform

**Figure 1.** Chemical structures and abbreviations of the linker ligands used in this study.

infrared spectroscopy (FTIR), UV-visible diffuse reflectance spectroscopy, scanning electron microscopy (SEM), and electric conductivity measurements.

## **■ EXPERIMENTAL SECTION**

**Materials.** All chemicals and solvents were purchased from Sigma Aldrich, AK Scientific, Fisher Scientific, and TCI America, and were used without further purification. Aqueous solutions were prepared using ultrapure (Type 1) water (resistivity 18.2 M $\Omega$ ·cm at 25 °C) from the Q-POD unit of the Milli-Q integral water purification system (Millipore, Billerica, MA, USA).

Synthesis of Ce-UiO-66-NO<sub>2</sub> (Ce-BDC-NO<sub>2</sub>). Ce-BDC-NO<sub>2</sub> was prepared with a slight modification to the reported procedures. <sup>23</sup> 820 mg of cerium (IV) ammonium nitrate was weighed in a glass vial. Add 3 mL of acetic acid and 8 mL of DI water into it, and magnetic stirring was performed at 600 rpm for 5 min. 1.6 mmol of 2-nitroterephthalic acid was added to the solution. The solution is then magnetically stirred at 600 rpm for 2 h at room temperature. The precipitates were then isolated *via* vacuum filtration, washed with water several times, and dried overnight under ambient conditions. The yield was ~696 mg.

**Synthesis of Ce-UiO-66 (Ce-BDC).** The synthesis of Ce-BDC is similar to that of Ce-BDC-NO $_2$ . 20 mL ethanol is added to the solution before the introduction of the terephthalic acid ligands. The yield was  $\sim$ 430 mg.

Synthesis of Ce-UiO-66-F<sub>4</sub> (Ce-BDC-F<sub>4</sub>). The synthesis of Ce-BDC-F<sub>4</sub> is similar to that of Ce-BDC. Tetrafluoroterephthalic acid is used instead of terephthalic acid ligands. The yield was  $\sim$ 495 mg.

Synthesis of Ce-UiO-66-dcbpy (Ce-dcbpy). Ce-dcbpy was prepared with a slight modification to the reported procedures.  $^{20,31}$  104.2 mg of 2,2′-bipyridine-5,5′-dicarboxylic acid (H<sub>2</sub>dcbpy) was weighed in a 20 mL glass vial and dissolved with 2.5 mL of DMF. To the solution of dcbpy, an aqueous solution of cerium (IV) ammonium nitrate (800  $\mu$ L, 0.533 M) was added. The glass vial was sealed and heated at 100 °C for 15 min under stirring. After cooling down to the room temperature, the yellow precipitates were collected *via* vacuum filtration, washed with DMF, and subjected to acetone washing for several times, and dried overnight under ambient conditions. The yield was ~102 mg.

Synthesis of Ce-UiO-66-bpdc (Ce-bpdc). The synthesis of Ce-bpdc is similar to that of Ce-dcbpy. 4,4'-Biphenyldicarboxylic acid ( $H_2$ bpdc) is used instead of  $H_2$ dcbpy.

**Synthesis of Ce-bpdc-dcbpy(1:1).** The synthesis of Ce-bpdc-dcbpy(1:1) is similar to that of Ce-dcbpy. 52.1 mg of  $H_2$ bpdc and 52.1 mg of  $H_2$ dcbpy were used for the synthesis of Ce-bpdc-dcbpy(1:1).

Synthesis of Ru-doped Ce-bpdc (MOF-1). 50 mg of Ce-bpdc and 6 mg of Ru(bpy)(dcbpy)Cl<sub>2</sub> were added in a 20 mL glass vial. Add 5 mL of ethanol and 5 mL of toluene into it. The mixture was heated at 90 °C for 24 h under magnetic stirring at 400 rpm. <sup>31</sup> The precipitates were then collected *via* vacuum filtration, washed with ethanol and acetone for several times, and dried overnight under ambient conditions. Yield: ~ 47 mg

Synthesis of Ru-doped Ce-bpdc-dcbpy(1:1) (MOF-2). 50 mg of Ce-bpdc-dcbpy(1:1) and 6 mg of Ru(bpy)(p-cymene)Cl<sub>2</sub> were added in a 20 mL glass vial. Add 5 mL of ethanol and 5 mL of toluene into it. The mixture was heated at 90 °C for 24 h under magnetic

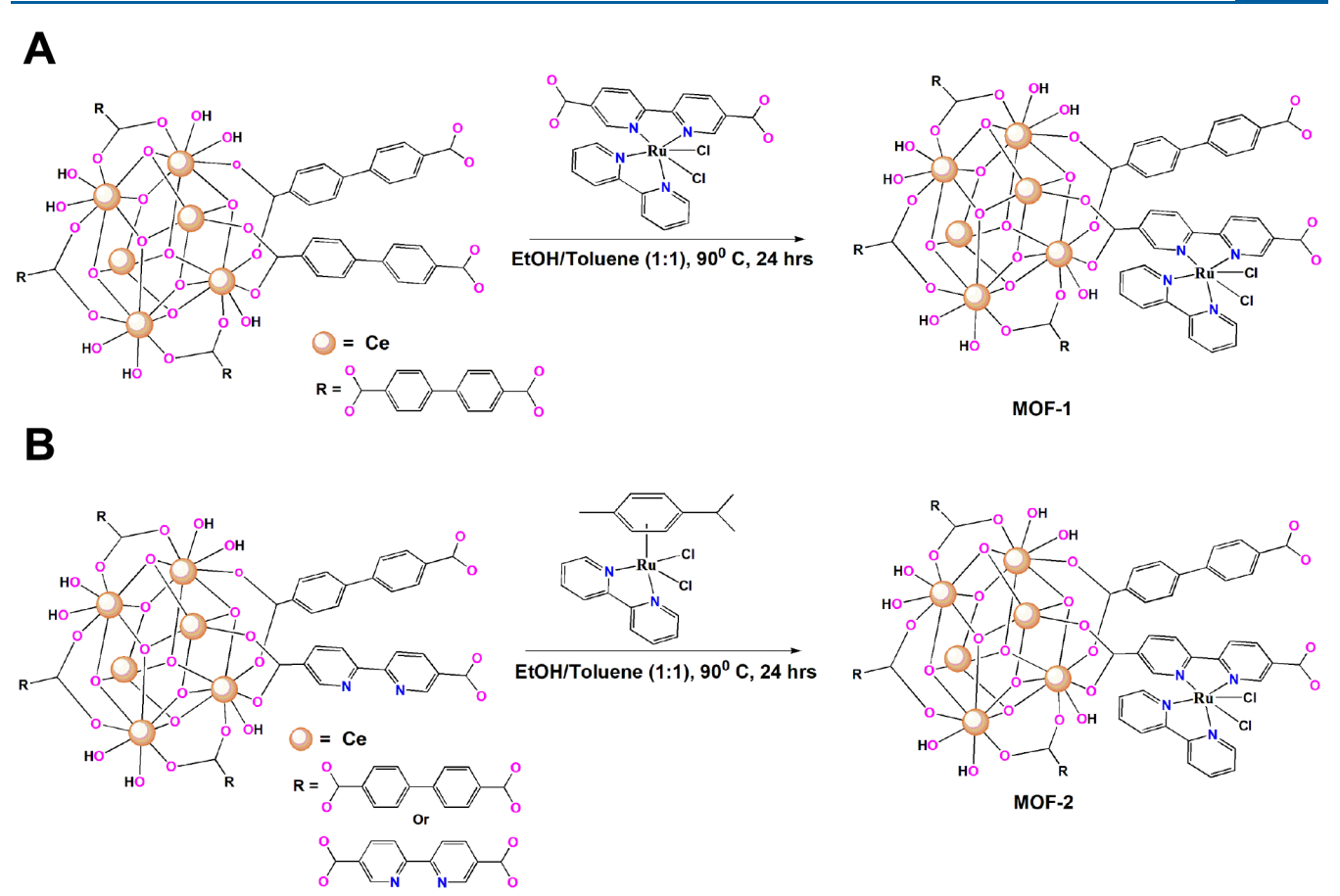


Figure 2. Synthetic scheme for the integration of a Ru catalyst into a Ce-MOF. (A) Linker exchange of Ce-bpdc with  $Ru(bpy)(dcbpy)Cl_2$  and (B) doping of Ru(bpy)(p-cymene) $Cl_2$  onto Ce-bpdc-dcbpy(1:1).

stirring at 400 rpm. The precipitates were then collected via vacuum filtration, washed with ethanol and acetone for several times, and dried overnight under ambient conditions. The yield was  $\sim$ 52 mg.

Physical Mixture of Ru(bpy)(p-cymene)Cl<sub>2</sub> and Ce-bpdc-dcbpy(1:1) (MOF-2-PM). 50 mg of Ce-bpdc-dcbpy(1:1) and 6 mg of Ru(bpy)(p-cymene)Cl<sub>2</sub> were ground using a mortar and pestle for 15 min. The physical mixture was taken, and an ink solution was made for photoelectrocatalytic measurements.

Safety comment: No uncommon hazards were noted during the experiments on the synthesis of samples and their characterization.

#### RESULTS

The Ru(bpy)(dcbpy)Cl<sub>2</sub> and Ru(bpy)(p-cymene)Cl<sub>2</sub> precursors were synthesized by following methods reported in the literature. Ce-MOFs with bpdc/dcbpy linkers were synthesized by reacting ceric ammonium nitrate with the linkers with ( $\sim$ 3:1,v/v) DMF:H<sub>2</sub>O solution at 100 °C. <sup>20,31</sup> The chemical structures and abbreviations of the ligands used for the synthesis of Ce-MOFs are shown in Figure 1.

The PXRD measurements were carried out to study the crystal structure of the as-synthesized materials. The measured PXRD patterns were compared with simulated patterns using existing crystallographic information from the Cambridge Crystallographic Data Centre (CCDC). Our synthesized Cebpdc, Ce-dcbpy, and Ce-bpdc-dcbpy(1:1) have crystalline structures (Figure S1), which are in agreement with the simulated PXRD patterns of Ce-UiO-66-dcbpy (CCDC 1509775). The PXRD patterns of Ce-BDC, Ce-BDC-F<sub>4</sub>, and Ce-BDC-NO $_2$  are given in Figure S2, which show the crystalline nature of the materials and match the simulated

PXRD patterns of Ce-UiO-66. The experimental PXRD patterns of Ce-MOFs with different linkers were in agreement with the simulated patterns, suggesting a relatively high purity and crystallinity of the synthesized Ce-MOFs.

The catalyst  $[Ru(bpy)(dcbpy)(H_2O)_2]^{2+}$  was introduced into the Ce-MOFs via two different methods: i) using a presynthesized Ru(bpy)(dcbpy)Cl<sub>2</sub> catalyst for ligand exchange (dcbpy of Ru-catalyst) with the Ce-bpdc MOF (MOF-1) (Figure 2A) or ii) using the precursor Ru(bpy)(pcymene)Cl<sub>2</sub>, allowing its reaction with the dcbpy-linker in the Ce-bpdc-dcbpy(1:1)<sup>6</sup> (MOF-2) (Figure 2B). Incorporating Ru-catalysts into the Ce-bpdc-dcbpy(1:1) MOF is facilitated by the presence of dcbpy, which effectively coordinates the Rucatalysts as compared to other single-ring BDC-based linkers. Both methods result in the incorporation of [Ru(bpy)(dcbpy)-(H<sub>2</sub>O)<sub>2</sub>]<sup>2+</sup> into Ce-MOF, enhancing the catalytic activity in water oxidation. The Ce-UiO-66 has an average pore diameter of  $\sim 15 \text{ Å}^{33}$  and [Ru(bpy)] moiety has a size of  $\sim 10 \text{ Å}^{6}$ , which should potentially allow the [Ru(bpy)] moiety to get inside the MOF pores during the synthesis. The crystalline nature of the Ce-MOFs remains the same after doping of the Ru catalyst into Ce-MOFs (Figure S3). The ratio of Ru precursor (Ru(bpy)(p-cymene)Cl<sub>2</sub> or Ru(bpy)(dcbpy)Cl<sub>2</sub>) to the linker was kept at ~1:12 based on our earlier findings for Fe MIL-126 MOF that such a ratio maintains the MOF crystalline structure.6

The electric conductivities of the as-synthesized Ce-MOFs were determined using a custom-made conductivity setup (Figure S4) and are tabulated in Tables 1 and S1. The Ce-

Table 1. The Electric Conductivity, Bandgap, and Photocatalytic Current Measured for Ce-MOFs

	electric conduc	tivity, $\sigma$ (S/cm)		photocatalytic current (A·cm <sup>-2</sup> )	
material	dark	light	direct bandgap (eV)	pH = 1	pH = 7
Ce-BDC	$2.44 \times 10^{-11}$	$3.00 \times 10^{-11}$	2.96	$1.0 \times 10^{-5}$	$9.26 \times 10^{-6}$
Ce-BDC-F <sub>4</sub>	$5.57 \times 10^{-6}$	$5.81 \times 10^{-6}$	2.82	$4.7 \times 10^{-5}$	$4.27 \times 10^{-5}$
Ce-BDC-NO <sub>2</sub>	$1.10 \times 10^{-7}$	$1.19 \times 10^{-7}$	3.06	$5.5 \times 10^{-5}$	$1.47 \times 10^{-5}$
Ce-bpdc	$1.40 \times 10^{-7}$	$1.62 \times 10^{-7}$	2.98	$5.4 \times 10^{-5}$	$2.85 \times 10^{-6}$
Ce-dcbpy	$1.73 \times 10^{-7}$	$1.94 \times 10^{-7}$	2.98	$9.6 \times 10^{-5}$	$9.15 \times 10^{-6}$
Ce-bpdc-dcbpy(1:1)	$0.91 \times 10^{-7}$	$1.10 \times 10^{-7}$	2.98	$1.7 \times 10^{-5}$	$7.57 \times 10^{-6}$

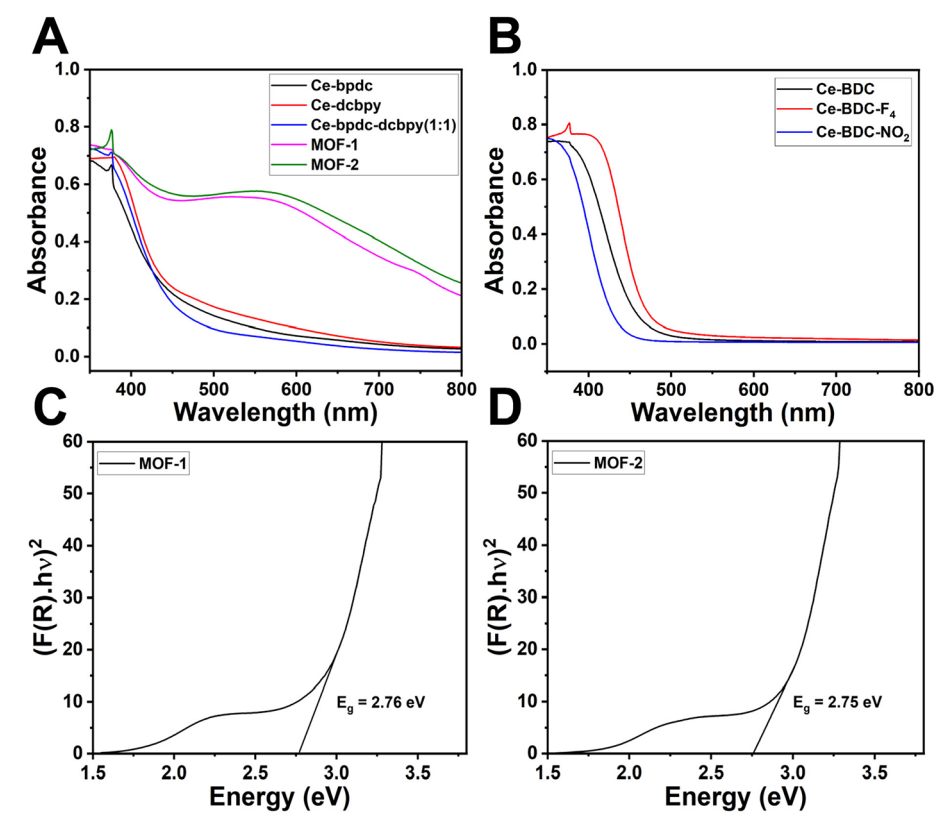


Figure 3. UV—vis diffuse reflectance spectra of (A) Ce-bpdc, Ce-dcbpy, Ce-bpdc-dcbpy(1:1), MOF-1, and MOF-2, and (B) Ce-BDC, Ce-BDC-F<sub>4</sub>, and Ce-BDC-NO<sub>2</sub> MOFs. Kubelka—Munk transformed reflectance spectra for (C) MOF-1 and (D) MOF-2. E<sub>g</sub> is a bandgap energy.

bpdc, Ce-dcbpy, and Ce-bpdc-dcbpy(1:1) samples show an electric conductivity  $\sim 10^{-7}$  S/cm, which is two orders of magnitude better than the reported Fe MIL-126 MOF (3.3  $\times$   $10^{-9}$  S/cm).<sup>6</sup> The electric conductivity of Ce-MOFs increased slightly under illumination (Tables 1 and S1).

Fourier transform infrared spectroscopy (FTIR) was used to measure the interaction between the Ce ions and the ligands. The FTIR spectra of Ce-bpdc, Ce-dcbpy, and Ce-bpdcdcbpy(1:1) are given in Figure S5A, which show the presence of carbonyl group vibrations in the 1300-1700 cm<sup>-1</sup> range and other bands characteristic of bpdc and dcbpy ligands (Table S2). 6,20 Meanwhile, for Ce-bpdc-dcbpy(1:1), the prominent two peaks observed at ~1592 cm<sup>-1</sup> and ~1395 cm<sup>-1</sup> are ascribed to the asymmetric and symmetric stretching vibrations of the coordinated carboxylic groups, respectively. 6,20 Figure S5B represents the FTIR spectra of Ce-BDC, Ce-BDC-F<sub>4</sub>, and Ce-BDC-NO<sub>2</sub>. The two prominent peaks at ~1500 cm<sup>-1</sup> ~1380 cm<sup>-1</sup> are vibrations of the terephthalate ion and carboxylate ions and the peak visible at 1538 cm<sup>-1</sup> for Ce-BDC-NO2 is assigned to asymmetric vibration of the nitro group (N-O).23 Additionally, the low-intensity bands observed

at 600 cm<sup>-1</sup> to 800 cm<sup>-1</sup> of the as-synthesized Ce-MOFs are due to the stretching vibrations of Ce-O. 22 The FTIR spectra of MOF-1 and MOF-2 are similar with those of the Ce-bpdc and Ce-bpdc-dcbpy(1:1), respectively (Figure S5C,D), which indicates that the MOFs remain unchanged with the doping of the Ru catalyst. Further, we carried out Raman spectroscopy of the as-synthesized MOFs at an excitation wavelength of 532 nm. The Raman spectra of the as-synthesized Ce-MOFs and Ru-doped Ce-MOFs are shown in Figure S6A-C. The Raman peaks at 300 cm<sup>-1</sup> to 600 cm<sup>-1</sup> are attributed to metal-ligand vibration of Ce-MOFs, and the Raman peak at 1100 cm<sup>-1</sup> to 1700 cm<sup>-1</sup> are corresponding to the vibrations associated with the organic ligands of Ce-MOFs. The Raman spectra of MOF-1 show the peaks of Ce-bpdc and Ru(bpy)(dcbpy)Cl<sub>2</sub> and those of the MOF-2 show the peaks of Ce-bpdcdcbpy(1:1) and Ru(bpy)(dcbpy)Cl<sub>2</sub> (Figure S6C), which indicates the successful incorporation of [Ru(bpy)(dcbpy)- $(H_2O)_2$ ]<sup>2+</sup> water oxidation catalyst into the Ce-MOF. The slight changes in the Raman spectra of MOF-1 and MOF-2 are mainly due to color differences and hence different enhancement in resonance Raman.

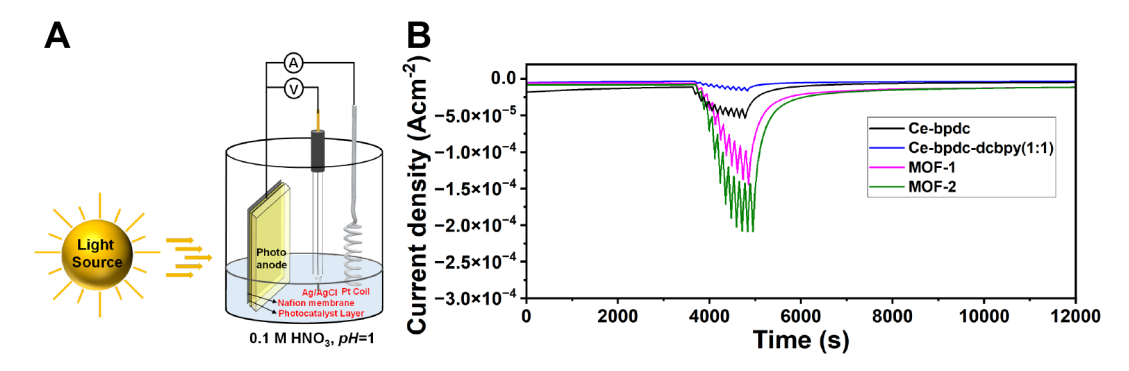


Figure 4. (A) Photoelectrochemical three-electrode setup with drop-casted MOF on FTO confined with the Nafion membrane, Ag/AgCl electrode, and Pt coil as working, reference, and counter electrodes, respectively, in 0.1 M HNO<sub>3</sub> electrolyte (pH = 1). (B) Chronoamperometry plots of Ce-bpdc, Ce-bpdc-dcbpy(1:1), MOF-1, and MOF-2 photoanodes at +1.4 V vs Ag/AgCl in 0.1 M HNO<sub>3</sub> (pH = 1). 10 light/dark cycles (1 min light/1 min dark) were applied after 60 min of the applied potential.

UV-vis diffuse reflectance spectroscopy is used to investigate the light absorption property of the as-synthesized materials. Figure 3A,B represents the UV-vis diffuse reflectance spectra of Ce-MOFs and Ru-doped Ce-MOFs, which illustrate the absorbance bands extending to the visible light region for all MOFs, with the intensity of absorbance increasing in the presence of Ru catalysts. The bandgaps of the MOFs were determined by converting the UV-vis diffuse reflectance spectra to Kubelka-Munk plots (detailed calculations are given in Supporting Information). The Kubelka-Munk plots of MOF-1 and MOF-2 are shown in Figure 3C,D, respectively. The Kubelka-Munk plots of all the Ce-MOFs in this study are given in Figure S7, and the bandgap of the MOFs are tabulated in Tables 1 and S3. The bandgap energy of the Ce-MOFs reported in this work matches that reported in the literature. 21-23,25 The UV-vis diffuse reflectance spectra of control samples; Zr-based UIO-67-dcbpy and Ru-doped UIO-67-dcbpy, are given in Figure S8. UIO-67-dcbpy lacks photoabsorbing ability to visible light, but for Ru-doped UIO-67-dcbpy, the absorption band extended to visible light and the intensity of absorbance increased in the presence of the Ru catalyst, similar to Ce-MOFs (Figure S8). For optimal utilization of visible light for water splitting, a photocatalyst should have a typical bandgap in the range of 2 to 3 eV.<sup>23</sup> All prepared Ce-MOFs satisfy this condition. 23,25 The bandgap for MOF-1 is 2.76 eV, and for MOF-2 is 2.75 eV due to the presence of a brightly colored (due to MLCT band) Ru<sup>II</sup> complex. However, under catalytic conditions, Ru is converted into a higher oxidation states of RuIII and RuIV, which are lightly colored. Thus, we do not consider the Ru center to participate as a chromophore, and the Ce-based node remains the photoabsorber in MOFs 1-2 passing the holes to the Rubased WOC. The same effect was established in Ru-containing Fe-based MOFs. We expect that when photoanodes are illuminated under an applied potential of +1.4 V vs Ag/AgCl, cerium nodes interconnected by ligands would effectively serve as a photoabsorber and Ru WOC would act as a catalyst for water oxidation at pH = 1.

An electrode was fabricated by drop-casting the ink prepared from Ce-MOFs or Ru-doped Ce-MOFs with Nafion solution as a binder on the FTO. To prepare a water splitting device, the electrode was firmly covered by a proton-conductive Nafion membrane (Figure 4A). Controlled electrocatalytic measurements were carried out using a three-electrode setup in 0.1 M HNO $_3$  (pH = 1). The Ce-MOFs, MOF-1, and MOF-2 with a proton-conductive Nafion membrane used as a

photoanode, and Ag/AgCl and Pt coil were used as reference and counter electrodes, respectively. The chemical and structural stability of the photoanode in the electrolyte is essential for ensuring its electrocatalytic activity toward prolonged electrolysis. To minimize dissolution effects, photoelectrochemical measurements are carried out by submerging the bottom of the photoanode in 0.1 M HNO<sub>3</sub>. Chronoamperometry was used for recording the photoactivity of the MOFs as the working anodes at the applied potential. Further, the activation process of drop-casted MOFs and saturation of the Nafion film was done at +1.4 V vs Ag/AgCl for 60 min. The photoelectrocatalytic performance of the MOFs was investigated with 1 min light on/off for 10 cycles, after 1 h of activation and ~24 h from the start of applied potential. Initially, we used a control study to examine the photoelectrocatalytic performance of Ce-MOFs without a Ru catalyst. The chronoamperometry plots of Ce-bpdc, Ce-dcbpy, Ce-bpdc-dcbpy(1:1), Ce-BDC, Ce-BDC-F<sub>4</sub>, and Ce-BDC- $NO_2$  photoanodes at +1.4 V vs Ag/AgCl at pH = 1 are shown in Figure S9, and the photocatalytic current of the Ce-MOFs are tabulated in Tables 1 and S4. All of the Ce-MOFs showed photoelectrocatalytic activity toward water oxidation with photocatalytic current in the order of  $\sim 10^{-5} \text{ A} \cdot \text{cm}^{-2}$ . The low current of Ce-MOFs photanodes is likely due to the low catalytic activity of Ce-MOFs in water oxidation at pH = 1. Zhixiong Guo et al. reported the photoinduced phase transition of Ce-UiO-66 observed via the color change of the Ce-UiO-66 suspensions from pale yellow (Ce<sup>IV</sup>) to brown (Ce<sup>III</sup>) during extended light exposure.<sup>13</sup> Herein, we did not observe any color change of the Ce-MOFs drop cast on the FTO electrode before and after the photoelectrocatalytic measurement, which indicated the stability of the material.

Further, in order to improve the photoelectrocatalytic activity, we incorporated the Ru catalyst into Ce-MOFs using two different methods using Ru(bpy)(dcbpy)Cl<sub>2</sub> and Ru(bpy)(p-cymene)Cl<sub>2</sub> precursors. Ru-doped Ce-MOFs showed enhanced photoelectrocatalytic activity for water oxidation in acidic conditions. The photocatalytic current increased by more than 1 order of magnitude for MOF-1 and MOF-2 under illumination, with MOF-1 and MOF-2 displaying a photocatalytic current of  $\sim 1.4 \times 10^{-4} \, \text{A} \cdot \text{cm}^{-2}$  and  $2.1 \times 10^{-4} \, \text{A} \cdot \text{cm}^{-2}$ , respectively, at +1.4 V vs Ag/AgCl in 0.1 M HNO<sub>3</sub> (Figures 4B, S10). To examine the stability of the photoelectrocatalyst, a prolonged electrolysis was conducted and photoelectrocatalytic activity was investigated again after  $\sim 24 \, \text{h}$  from the start of the applied potential. The MOF-1

and MOF-2 exhibited a photocatalytic current of  $\sim 1.3 \times 10^{-4}$  $A \cdot cm^{-2}$  and  $2.3 \times 10^{-4} \, A \cdot cm^{-2}$ , respectively, which showed the long-term durability of the materials even after ~24 h of chronoamperometry test without any significant loss of photocurrent (Figure S10). As a control study, the physical mixture of Ce-bpdc-dcbpy(1:1) and Ru(bpy)(p-cymene)Cl<sub>2</sub> was made (MOF-2-PM) and photoelectrocatalytic measurement was carried out under the same conditions as those of Ce-MOFs. MOF-2-PM showed a photocatalytic current of  $\sim 6.5 \times 10^{-5} \text{ A} \cdot \text{cm}^{-2} \text{ at } +1.4 \text{ V vs Ag/AgCl in } 0.1 \text{ M HNO}_3$ (Figure S11), which is lower as compared to the MOF-2. This indicates that the physical mixing of the samples does not enhance the photoelectrocatalytic activity due to the lack of a formed electrocatalyst in the photoabsorbing material. Further, we studied the photoelectrocatalytic performance of MOF-1 and MOF-2 under pH = 7 in a three-electrode setup without a proton-conductive Nafion membrane. Both MOF-1 and MOF-2 showed the current density of  $\sim 10^{-4} \text{ A} \cdot \text{cm}^{-2}$  at + 1.4 V vs Ag/AgCl in 0.1 M phosphate buffer (pH = 7) (Figure S12).

"Thus, no activity improvement was found at pH = 7. This is similar to the earlier observations that an Fe-based MOF with  $[Ru(bpy)(dcbpy)(H_2O)_2]^{2+}$  catalyst did not show improvement in current at pH = 7. This is likely due to the limitations of the Ru catalyst or local acidification of the pores with a catalyst at pH = 7.

Further, we performed a control study of chronoamperometry measurement on  $[Ru(bpy)(dcbpy)(H_2O)_2]^{2+}$ -doped UIO-67-dcbpy (~1:12 ratio of Ru catalyst to the dcbpy linker) with 1 min light on/off for 10 cycles, after 1 h of activation at +1.4 V vs Ag/AgCl in 0.1 M HNO3. UIO-67-dcbpy lacks photoabsorption in the visible light owing to its wide band gap energy. The measured photoelectrocatalytic current of Ru(bpy)(dcbpy)-doped UIO-67-dcbpy is notably lower as compared to MOF-2 (Figure S13), which suggests that the [Ru(bpy)(dcbpy)] part in Ru-doped UIO-67-dcbpy cannot function as an effective light absorbing unit for photoelectrochemical water splitting.  $^6$ 

To examine the structural stability of the catalyst during photoelectrocatalysis, we carried out the post-catalysis characterizations (FTIR and SEM) for MOF-1 and MOF-2. Figure S14 displays the SEM images of MOF-1 and MOF-2 before and after the 24 h photoelectrocatalytic chronoamperometry test in acidic media. Remarkably, the morphology of MOF-1 and MOF-2 remains largely unchanged even after the 24 h stability test, suggesting the structural stability of the materials. Figure S15 illustrates the FTIR spectra of MOF-1 and MOF-2 before and after the 24 h stability test in acidic media. There was no significant change in the FTIR peak position of MOF-1 and MOF-2 after the photoelectrocatalysis, further indicating the material stability.

# DISCUSSION

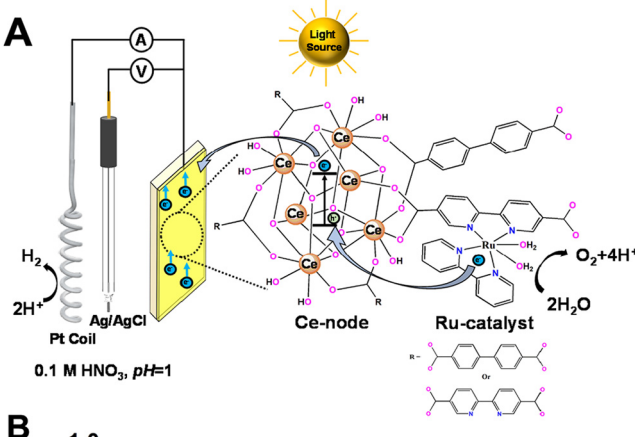
Metal—organic frameworks (MOFs) have emerged as a platform for the realization of integrated devices for artificial photosynthesis, <sup>15,18,34–43</sup> because of their large surface areas, adaptability, stability, and, in some instances, photocatalytic properties. <sup>44</sup> Notably, certain WOCs based on Ir and Ru have been incorporated into UiO-67 and NU-1000 (NU = Northwestern University) <sup>17,44–46</sup> MOFs, enhancing electrocatalytic water oxidation activity. However, these systems currently lack light absorption capabilities. <sup>44,47–49</sup> Developing cost-effective and highly efficient photoelectrocatalysts for water splitting under light activation is yet challenging. A few

Ce-based MOFs have been reported for photocatalytic water splitting and photocatalytic water splitting with CO<sub>2</sub> reduction at moderate pH. 23,31 Water oxidation in MOFs under illumination can be investigated as a multistep process similar to the mechanisms observed in natural photosynthesis. Generally, the first step for photocatalytic water oxidation is the absorption of incident photons by the photoactive material followed by the splitting of water by an catalytically active center. If the bandgap energy of the photoactive material is lower than the energy of the incident photon, it generates the electron-hole pair. Holes are expected to migrate to the catalytic sites to drive the water splitting reaction. However, one prominent challenge is the occurrence of charge recombination, which diminishes the overall efficiency of photocatalytic systems. Ce-based MOFs were shown to be efficient in preventing the recombination of photogenerated electrons and holes, making them an ideal candidate for photoelectrocatalysis.<sup>22,23</sup>

The substitution of the benzene moiety with a bipyridine ligand proved crucial, enabling the development of a chelating framework capable of binding transition metal coordination compounds. This immobilization of active WOC within the MOF significantly enhances its catalytic activity. The incorporation of  $[Ru(bpy)(dcbpy)(H_2O)_2]^{2+}$  catalytic unit into Fe-MOFs either by linker exchange or doping of the precursor  $(Ru(bpy)(p\text{-cymene})Cl_2)$  was reported earlier. The doping strategy is designed to achieve an enhanced photocatalytic water oxidation activity by facilitating the transfer of electrons from immobilized Ru-catalysts to light-activated Fenodes of the MOF. In this study, we found that the incorporation of  $[Ru(bpy)(dcbpy)(H_2O)_2]^{2+}$  in Ce-based MOFs (MOF-1 and MOF-2) increases the activity in photocatalytic water oxidation.

The band position for the UiO-66-dcbpy Ce-MOF is reported by Karmakar et al.<sup>31</sup> In our study, as the Ce-MOF cluster is the same as reported by Karmakar et al., we have taken the value of the conduction band position and calculated the valence band position for our MOF from the band gap value (Tables 1 and S3). The energy diagram of the Ce-MOF is given in Figure 5B. In our previous study, we reported the electrochemistry of the [Ru(bpy)(dcbpy)(H<sub>2</sub>O)<sub>2</sub>]<sup>2+</sup> WOC.<sup>17</sup> The oxidation potentials of  $[Ru(bpy)(dcbpy)(H_2O)_2]^{2+}$  are ~1.02 V, ~1.09 V, and ~1.53 V vs NHE for Ru<sup>II</sup>/Ru<sup>III</sup>, Ru<sup>III</sup>/Ru<sup>IV</sup>, and Ru<sup>IV</sup>/Ru<sup>V</sup> redox couple, respectively, at pH = 1, and RuV is the active intermediate for water splitting. Herein, we performed the photoelectrocatalysis using Ru(bpy)(dcbpy)doped Ce-MOFs at the applied potential of +1.6 V vs NHE at pH = 1, which is high enough to convert the Ru-catalyst to Ru<sup>V</sup> species to ease the water oxidation reaction. Hence [Ru(bpy)- $(dcbpy)(H_2O)_2$ <sup>2+</sup> acts as a WOC and not as a photosensitizer. According to the literature, we found that Ce-MOFs (without catalyst) are capable of absorbing visible light and generating electron-hole pairs. Following this, the electron is transferred from the catalytic Ru center to electron vacancies (holes) in the Ce-MOFs and later to the electrode, which further facilitates the water splitting process (Figure 5).

MOF-1 and MOF-2 exhibit high current densities for water oxidation in acidic conditions under illumination. This indicates the enhanced photocatalytic water oxidation activity of Ru-WOC Ce-MOFs, which is also comparable with the reported Fe-based MOFs (Table 2).<sup>6</sup> We calculated theoretically the amount of hydrogen evolved from the chronoamperometry plot during light illumination. Ce-bpdc-dcbpy(1:1)



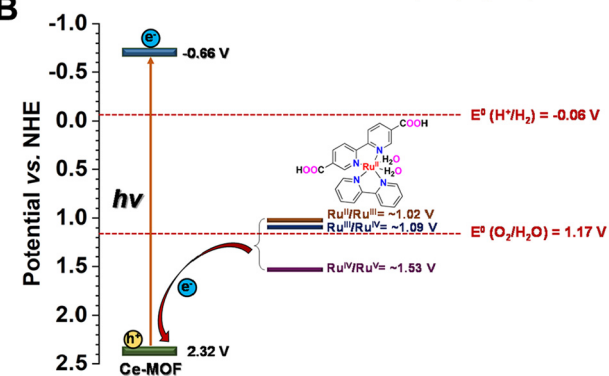


**Figure 5.** (A) Schematic representation of the proposed photoelectrocatalytic water oxidation mechanism of Ru-doped Ce-MOFs and (B) energy level diagram of Ce-MOFs showing a possible charge transfer mechanism. Required potential for the HER or OER vs NHE at pH = 1 is marked in the figure. The oxidation potentials of  $[Ru(bpy)(dcbpy)(H_2O)_2]^{2+}$  are  $\sim\!1.02$  V,  $\sim\!1.09$  V, and  $\sim\!1.53$  V vs NHE for  $Ru^{\rm II}/Ru^{\rm III}$ ,  $Ru^{\rm III}/Ru^{\rm IV}$ , and  $Ru^{\rm IV}/Ru^{\rm V}$  redox couple, respectively at pH = 1.

exhibits a low photocatalytic hydrogen evolution of 4.1  $\mu$ mol h<sup>-1</sup> at pH = 1 (8 mg of MOF having a geometrical area of 1 cm<sup>2</sup>). In contrast, **MOF-1** and **MOF-2** show higher photocatalytic hydrogen evolution of 25.8  $\mu$ mol h<sup>-1</sup> and 40.4  $\mu$ mol h<sup>-1</sup>, respectively at pH = 1, which is better than that of the reported Pt/Ce-UiO-66-NH<sub>2</sub> system. <sup>23</sup>

The cost-effective and catalytically active Ru-WOC Ce-MOFs are promising candidates for light-driven water oxidation, particularly under acidic conditions. This development opens a new pathway for the advancement of such systems designed for sustainable water-splitting processes.

#### CONCLUSION

In conclusion, the  $[Ru(bpy)(dcbpy)(H_2O)_2]^{2+}$  catalytic unit was successfully incorporated into Ce-based MOFs (MOF-1 and MOF-2). The strategic substitution of benzene moieties with bipyridine ligands allowed the immobilization of an active water oxidation catalyst, enhancing the catalytic activity. Rudoped Ce-MOFs exhibit a high current density comparable with the reported  $[Ru(bpy)(dcbpy)(H_2O)_2]^{2+}$  Fe MIL-126 MOF for water oxidation under acidic conditions. This study marks a significant milestone in advancing the sustainable energy technologies, offering promising options for environmentally conscious and economically viable photoelectrocatalysts. The success of Ru-WOC Ce-MOFs positions them as key contributors to a cleaner and more sustainable energy future.

#### ASSOCIATED CONTENT

# **5** Supporting Information

The Supporting Information is available free of charge at https://pubs.acs.org/doi/10.1021/acs.inorgchem.3c04632.

PXRD patterns, conductivity measurements, FTIR spectra, Raman spectra, UV-vis diffuse reflectance spectra, chronoamperometry plot and SEM images (PDF)

## AUTHOR INFORMATION

#### **Corresponding Author**

Yulia Pushkar — Department of Physics and Astronomy, Purdue University, West Lafayette, Indiana 47907, United States; orcid.org/0000-0001-7949-6472; Email: ypushkar@purdue.edu

#### **Authors**

Naduvile Purayil Dileep — Department of Physics and Astronomy, Purdue University, West Lafayette, Indiana 47907, United States; orcid.org/0009-0005-1575-8038

Jully Patel — Department of Physics and Astronomy, Purdue University, West Lafayette, Indiana 47907, United States; orcid.org/0000-0002-4008-2165

Complete contact information is available at: https://pubs.acs.org/10.1021/acs.inorgchem.3c04632

#### Notes

The authors declare no competing financial interest.

# ACKNOWLEDGMENTS

This research was supported by NSF, CHE-2155060 (Y.P.). We thank Dr. Alexei Lagoutchev from Birck Nanotechnology

Table 2. Comparison of the Current Densities Shown by Different Mononuclear Ru Complex-Doped MOFs

type of system	potential (V vs Ag/AgCl)	current density (A·cm <sup>-2</sup> )	pН	references
UIO-67@[Ru(tpy)(dcbpy)( $H_2O$ )] <sup>2+</sup>	1.5	$7.1 \times 10^{-5}$	~7	36
UIO-67@[Ru(tpy)(dcbpy)( $H_2O$ )] <sup>2+</sup>	1.5	$1.1 \times 10^{-5}$	~8	45
UIO-67@[Ru(bpy)(dcbpy)( $H_2O$ ) <sub>2</sub> ] <sup>2+</sup>	1.4	$2.5 \times 10^{-5}$	1	17
MIL-126@[Ru(bpy)(dcbpy)( $H_2O$ ) <sub>2</sub> ] <sup>2+</sup>	1.4	$^{a}6.5 \times 10^{-4}$	1	6
$NU-1000@[Ru(tda)(py(PhCOOH)_2)_2]$	1.1	$1.8 \times 10^{-4}$	7	46
MOF-1	1.4	$a^{1.4} \times 10^{-4}$	1	this work
MOF-2	1.4	$a^{2}.1 \times 10^{-4}$	1	
MOF-1	1.4	$a^{1}1.0 \times 10^{-4}$	7	
MOF-2	1.4	$^{a}1.0 \times 10^{-4}$	7	

<sup>&</sup>lt;sup>a</sup>Photoelectrocatalytic current measured under illumination.

Center, Purdue University for providing training for the Lambda 950 UV—vis spectrophotometer. We thank Dr. Olga Maximova for assistance with SEM measurements.

#### REFERENCES

- (1) Hunter, B. M.; Gray, H. B.; Müller, A. M. Earth-Abundant Heterogeneous Water Oxidation Catalysts. *Chem. Rev.* **2016**, *116* (22), 14120–14136.
- (2) Patel, J.; Bury, G.; Ravari, A. K.; Ezhov, R.; Pushkar, Y. Systematic Influence of Electronic Modification of Ligands on the Catalytic Rate of Water Oxidation by a Single-Site Ru-Based Catalyst. *ChemSuschem* **2022**, *15* (4), No. e202101657.
- (3) Dileep, N. P.; Puthenveettil, L. K.; Myakala, S. N.; Shaijumon, M. M. Electrophoretically-Deposited BiSbSe<sub>3</sub> Nanoparticles as Highly Efficient Electrocatalysts for Hydrogen Evolution Reaction. *Appl. Mater. Today* **2022**, *27*, 101502.
- (4) Farooq, U.; Ahmad, T.; Naaz, F.; Islam, S. U. Review on Metals and Metal Oxides in Sustainable Energy Production: Progress and Perspectives. *Energy Fuels* **2023**, *37* (3), 1577–1632.
- (5) Han, H.; Jang, J. U.; Oh, D.; Na, K.-H.; Choi, W.-Y.; Jayakrishnan, N.; Nayak, A. K. Advances and Perspectives of Titanium-Based Nanocomposites for Energy Generation and Environmental Remediation Applications: A Review. *Energy Fuels* **2023**, *37*, 17708.
- (6) Ezhov, R.; Ravari, A. K.; Palenik, M.; Loomis, A.; Meira, D. M.; Savikhin, S.; Pushkar, Y. Photoexcitation of  $Fe_3O$  Nodes in MOF Drives Water Oxidation at pH=1 When Ru Catalyst Is Present. ChemSuschem 2023, 16 (5), No. e202202124.
- (7) Lee, Y.; Suntivich, J.; May, K. J.; Perry, E. E.; Shao-Horn, Y. Synthesis and Activities of Rutile IrO<sub>2</sub> and RuO<sub>2</sub> Nanoparticles for Oxygen Evolution in Acid and Alkaline Solutions. *J. Phys. Chem. Lett.* **2012**, *3* (3), 399–404.
- (8) Kirshenbaum, M. J.; Richter, M. H.; Dasog, M. Electrochemical Water Oxidation in Acidic Solution Using Titanium Diboride (TiB<sub>2</sub>) Catalyst. *ChemCatchem* **2019**, *11* (16), 3877–3881.
- (9) Navalón, S.; Dhakshinamoorthy, A.; Álvaro, M.; Ferrer, B.; García, H. Metal-Organic Frameworks as Photocatalysts for Solar-Driven Overall Water Splitting. *Chem. Rev.* **2023**, *123* (1), 445–490.
- (10) Suremann, N. F.; McCarthy, B. D.; Gschwind, W.; Kumar, A.; Johnson, B. A.; Hammarström, L.; Ott, S. Molecular Catalysis of Energy Relevance in Metal-Organic Frameworks: From Higher Coordination Sphere to System Effects. *Chem. Rev.* **2023**, *123* (10), 6545–6611.
- (11) Naghdi, S.; Shahrestani, M. M.; Zendehbad, M.; Djahaniani, H.; Kazemian, H.; Eder, D. Recent Advances in Application of Metal-Organic Frameworks (MOFs) as Adsorbent and Catalyst in Removal of Persistent Organic Pollutants (POPs). *J. Hazard. Mater.* **2023**, 442, 130127.
- (12) Yu, L.; Liu, Y.; Zhou, M. Improved Electrochemiluminescence Labels for Heterogeneous Microbead Immunoassay. *Anal. Bioanal. Chem.* **2016**, 408 (25), 7095–7103.
- (13) Guo, Z.; Luo, Q.-C.; Qin, L.; Tian, Z.; Zheng, Y.-Z.; Ma, Y.; Qu, Y. Photoinduced Phase Transition of Ce-UiO-66 to Ce-BDC-OH. *Inorg. Chem.* **2022**, *61* (25), 9557–9563.
- (14) Pullen, S.; Ott, S. Photochemical Hydrogen Production with Metal-Organic Frameworks. *Top. Catal.* **2016**, *59* (19), 1712–1721.
- (15) Majewski, M. B.; Peters, A. W.; Wasielewski, M. R.; Hupp, J. T.; Farha, O. K. Metal-Organic Frameworks as Platform Materials for Solar Fuels Catalysis. *ACS Energy Lett.* **2018**, 3 (3), 598–611.
- (16) Musho, T.; Li, J.; Wu, N. Band Gap Modulation of Functionalized Metal-Organic Frameworks. *Phys. Chem. Chem. Phys.* **2014**, *16* (43), 23646–23653.
- (17) Ezhov, R.; Karbakhsh Ravari, A.; Page, A.; Pushkar, Y. Water Oxidation Catalyst Cis-[Ru(Bpy)(5,5'-Dcbpy)(H<sub>2</sub>O)<sub>2</sub>]<sup>2+</sup> and Its Stabilization in Metal-Organic Framework. *ACS Catal.* **2020**, *10* (9), 5299–5308.
- (18) Horiuchi, Y.; Toyao, T.; Miyahara, K.; Zakary, L.; Van, D. D.; Kamata, Y.; Kim, T.-H.; Lee, S. W.; Matsuoka, M. Visible-Light-

- Driven Photocatalytic Water Oxidation Catalysed by Iron-Based Metal-Organic Frameworks. *Chem. Commun.* **2016**, 52 (29), 5190–5193.
- (19) Chi, L.; Xu, Q.; Liang, X.; Wang, J.; Su, X. Iron-Based Metal-Organic Frameworks as Catalysts for Visible Light-Driven Water Oxidation. *Small* **2016**, *12* (10), 1351–1358.
- (20) Lammert, M.; Glißmann, C.; Reinsch, H.; Stock, N. Synthesis and Characterization of New Ce(IV)-MOFs Exhibiting Various Framework Topologies. *Cryst. Growth Des.* **2017**, *17* (3), 1125–1131.
- (21) Melillo, A.; Cabrero-Antonino, M.; Ferrer, B.; Dhakshinamoorthy, A.; Baldoví, H. G.; Navalón, S. MOF-on-MOF Composites with UiO-66-Based Materials as Photocatalysts for the Overall Water Splitting under Sunlight Irradiation. *Energy Fuels* **2023**, 37 (7), 5457–5468.
- (22) Yang, H.; Jia, L.; Zhang, Z.; Xu, B.; Liu, Z.; Zhang, Q.; Cao, Y.; Nan, Z.; Zhang, M.; Ohno, T. Novel Cerium-Based MOFs Photocatalyst for Photocarrier Collaborative Performance under Visible Light. *J. Catal.* **2022**, *405*, 74–83.
- (23) Dai, S.; Montero-Lanzuela, E.; Tissot, A.; Baldoví, H. G.; García, H.; Navalón, S.; Serre, C. Room Temperature Design of Ce(IV)-MOFs: From Photocatalytic HER and OER to Overall Water Splitting under Simulated Sunlight Irradiation. *Chem. Sci.* **2023**, *14* (13), 3451–3461.
- (24) Song, Y.; Pi, Y.; Feng, X.; Ni, K.; Xu, Z.; Chen, J. S.; Li, Z.; Lin, W. Cerium-Based Metal-Organic Layers Catalyze Hydrogen Evolution Reaction through Dual Photoexcitation. *J. Am. Chem. Soc.* **2020**, 142 (15), 6866–6871.
- (25) Campanelli, M.; Del Giacco, T.; De Angelis, F.; Mosconi, E.; Taddei, M.; Marmottini, F.; D'Amato, R.; Costantino, F. Solvent-Free Synthetic Route for Cerium(IV) Metal-Organic Frameworks with UiO-66 Architecture and Their Photocatalytic Applications. *ACS Appl. Mater. Interfaces* **2019**, *11* (48), 45031–45037.
- (26) Ho, W. H.; Li, S. C.; Wang, Y. C.; Chang, T. E.; Chiang, Y. T.; Li, Y. P.; Kung, C. W. Proton-Conductive Cerium-Based Metal-Organic Frameworks. ACS Appl. Mater. Interfaces 2021, 13 (46), 55358–55366.
- (27) Goudarzi, M. D.; Khosroshahi, N.; Safarifard, V. Exploring Novel Heterojunctions Based on the Cerium Metal-Organic Framework Family and CAU-1, as Dissimilar Structures, for the Sake of Photocatalytic Activity Enhancement. *RSC Adv.* **2022**, *12* (50), 32237–32248.
- (28) Shen, C. H.; Chuang, C. H.; Gu, Y. J.; Ho, W. H.; Song, Y. D.; Chen, Y. C.; Wang, Y. C.; Kung, C. W. Cerium-Based Metal-Organic Framework Nanocrystals Interconnected by Carbon Nanotubes for Boosting Electrochemical Capacitor Performance. ACS Appl. Mater. Interfaces 2021, 13 (14), 16418–16426.
- (29) Jacobsen, J.; Ienco, A.; D'Amato, R.; Costantino, F.; Stock, N. The Chemistry of Ce-Based Metal-Organic Frameworks. *Dalt. Trans.* **2020**, 49 (46), 16551–16586.
- (30) Zhang, C.; Xu, Y.; Lv, C.; Zhou, X.; Wang, Y.; Xing, W.; Meng, Q.; Kong, Y.; Chen, G. Mimicking  $\pi$  Backdonation in Ce-MOFs for Solar-Driven Ammonia Synthesis. *ACS Appl. Mater. Interfaces* **2019**, 11 (33), 29917–29923.
- (31) Karmakar, S.; Barman, S.; Rahimi, F. A.; Biswas, S.; Nath, S.; Maji, T. K. Developing Post-Modified Ce-MOF as a Photocatalyst: A Detail Mechanistic Insight into CO<sub>2</sub> Reduction toward Selective C2 Product Formation. *Energy Environ. Sci.* **2023**, *16* (5), 2187–2198.
- (32) Wen, M.; Kuwahara, Y.; Mori, K.; Zhang, D.; Li, H.; Yamashita, H. Synthesis of Ce Ions Doped Metal-Organic Framework for Promoting Catalytic H<sub>2</sub> Production from Ammonia Borane under Visible Light Irradiation. *J. Mater. Chem. A* **2015**, 3 (27), 14134–14141
- (33) Ebrahim, A. M.; Bandosz, T. J. Ce(III) Doped Zr-Based MOFs as Excellent NO<sub>2</sub> Adsorbents at Ambient Conditions. ACS Appl. Mater. Interfaces 2013, 5 (21), 10565–10573.
- (34) Feng, J.; Li, X.; Luo, Y.; Su, Z.; Zhong, M.; Yu, B.; Shi, J. Microenvironment Regulation of Ru(Bda)L<sub>2</sub> Catalyst Incorporated in Metal-Organic Framework for Effective Photo-Driven Water Oxidation. *Chin. J. Catal.* **2023**, 48, 127–136.

- (35) Moore, S. C.; Smith, M. R.; Trettin, J. L.; Yang, R. A.; Sarazen, M. L. Kinetic Impacts of Defect Sites in Metal-Organic Framework Catalysts under Varied Driving Forces. *ACS Energy Lett.* **2023**, 8 (3), 1397–1407.
- (36) Lin, S.; Pineda-Galvan, Y.; Maza, W. A.; Epley, C. C.; Zhu, J.; Kessinger, M. C.; Pushkar, Y.; Morris, A. J. Electrochemical Water Oxidation by a Catalyst-Modified Metal-Organic Framework Thin Film. *ChemSuschem* **2017**, *10* (3), 514–522.
- (37) Wan, H.; Ma, R.; Liu, X.; Pan, J.; Wang, H.; Liang, S.; Qiu, G.; Sasaki, T. Rare Cobalt-Based Phosphate Nanoribbons with Unique 5-Coordination for Electrocatalytic Water Oxidation. *ACS Energy Lett.* **2018**, 3 (6), 1254–1260.
- (38) Yang, S.; Pattengale, B.; Lee, S.; Huang, J. Real-Time Visualization of Active Species in a Single-Site Metal-Organic Framework Photocatalyst. *ACS Energy Lett.* **2018**, 3 (3), 532–539.
- (39) Li, J.; Huang, W.; Wang, M.; Xi, S.; Meng, J.; Zhao, K.; Jin, J.; Xu, W.; Wang, Z.; Liu, X.; et al. Low-Crystalline Bimetallic Metal-Organic Framework Electrocatalysts with Rich Active Sites for Oxygen Evolution. ACS Energy Lett. 2019, 4 (1), 285–292.
- (40) Zahran, Z. N.; Tsubonouchi, Y.; Mohamed, E. A.; Yagi, M. Recent Advances in the Development of Molecular Catalyst-Based Anodes for Water Oxidation toward Artificial Photosynthesis. *ChemSuschem* **2019**, 12 (9), 1775–1793.
- (41) Luo, H.; Zeng, Z.; Zeng, G.; Zhang, C.; Xiao, R.; Huang, D.; Lai, C.; Cheng, M.; Wang, W.; Xiong, W.; et al. Recent Progress on Metal-Organic Frameworks Based- and Derived-Photocatalysts for Water Splitting. *Chem. Eng. J.* **2020**, 383, 123196.
- (42) Mukhopadhyay, S.; Basu, O.; Nasani, R.; Das, S. K. Evolution of Metal Organic Frameworks as Electrocatalysts for Water Oxidation. *Chem. Commun.* **2020**, *56* (79), 11735–11748.
- (43) Zheng, W.; Lee, L. Y. S. Metal—Organic Frameworks for Electrocatalysis: Catalyst or Precatalyst? *ACS Energy Lett.* **2021**, *6* (8), 2838—2843.
- (44) Wang, C.; Wang, J.-L.; Lin, W. Elucidating Molecular Iridium Water Oxidation Catalysts Using Metal-Organic Frameworks: A Comprehensive Structural, Catalytic, Spectroscopic, and Kinetic Study. J. Am. Chem. Soc. 2012, 134 (48), 19895–19908.
- (45) Johnson, B. A.; Bhunia, A.; Ott, S. Electrocatalytic Water Oxidation by a Molecular Catalyst Incorporated into a Metal-Organic Framework Thin Film. *Dalt. Trans.* **2017**, *46* (5), 1382–1388.
- (46) Howe, A.; Liseev, T.; Gil-Sepulcre, M.; Gimbert-Suriñach, C.; Benet-Buchholz, J.; Llobet, A.; Ott, S. Electrocatalytic Water Oxidation from a Mixed Linker MOF Based on NU-1000 with an Integrated Ruthenium-Based Metallo-Linker. *Mater. Adv.* **2022**, 3 (10), 4227–4234.
- (47) Hull, J. F.; Balcells, D.; Blakemore, J. D.; Incarvito, C. D.; Eisenstein, O.; Brudvig, G. W.; Crabtree, R. H. Highly Active and Robust Cp\* Iridium Complexes for Catalytic Water Oxidation. *J. Am. Chem. Soc.* **2009**, *131* (25), 8730–8731.
- (48) Blakemore, J. D.; Schley, N. D.; Balcells, D.; Hull, J. F.; Olack, G. W.; Incarvito, C. D.; Eisenstein, O.; Brudvig, G. W.; Crabtree, R. H. Half-Sandwich Iridium Complexes for Homogeneous Water-Oxidation Catalysis. *J. Am. Chem. Soc.* **2010**, *132* (45), 16017–16029. (49) Wang, C.; Xie, Z.; deKrafft, K. E.; Lin, W. Doping Metal-Organic Frameworks for Water Oxidation, Carbon Dioxide Reduction, and Organic Photocatalysis. *J. Am. Chem. Soc.* **2011**, *133* (34), 13445–13454.